PHYSICAL REVIEW D **75,** 024034 (2007)

Gravitational-wave background from compact objects embedded in active galactic nuclei accretion disks

Günter Sigl

APC UMR 7164 (CNRS, Université Paris 7, CEA, Observatoire de Paris) (AstroParticules et Cosmologie),
10, rue Alice Domon et Léonie Duquet, 75205 Paris Cedex 13, France
Institut d'Astrophysique de Paris, 98bis Boulevard Arago, 75014 Paris, France

Jeremy Schnittman and Alessandra Buonanno

Physics Department, University of Maryland, College Park, Maryland 20742, USA

(Received 23 October 2006; published 26 January 2007)

We consider a model in which massive stars form in a self-gravitating accretion disk around an active galactic nucleus (AGN). These stars may evolve and collapse to form compact objects on a time scale shorter than the accretion time, thus producing an important family of sources for LISA. Assuming the compact object formation/inspiral rate is proportional to the steady-state gas accretion rate, we use the intrinsic hard x ray AGN luminosity function to estimate expected event rates and signal strengths. We find that these sources will produce a continuous low-frequency ($\lesssim 1$ mHz) background detectable by LISA if more than $\sim 1\%$ of the accreted matter is in the form of compact objects. For compact objects with masses $\gtrsim 10 M_\odot$, the last stages of the inspiral events should be resolvable above a few mHz, with rates as high as a few hundred per year.

DOI: 10.1103/PhysRevD.75.024034 PACS numbers: 04.30.Db, 04.80.Nn, 98.54.Cm, 98.70.Sa

I. INTRODUCTION AND MOTIVATION

Some time in the near future, the launch and operation of the laser interferometer space antenna (LISA) [1] will issue in a new age of gravitational-wave (GW) astronomy. One of the major challenges that will face GW astronomers is the successful discrimination between instrumental noise, stochastic GW backgrounds, and individual, resolvable GW sources. For example, the population of galactic white-dwarf binaries in close orbits will provide a major contribution to the LISA noise curve in the 0.1–1 mHz band [2]. At the same time, this confusion "noise" can also be treated as a signal, and its shape and amplitude will provide important information about the distribution and properties of white-dwarf binaries in the galaxy (e.g. Ref. [3]).

It has recently been proposed that, in the self-gravitating outer regions of accretion disks of active galactic nuclei (AGN), massive stars could form and evolve, eventually collapsing into compact objects and merging with the central black hole [4,5]. This final inspiral stage would be an important source of GWs in the LISA band. Depending on the specific properties of the accretion disk and the embedded compact objects, this population could contribute to the GW background and also produce individual resolvable signals. It is therefore a matter of theoretical and practical interest to understand the nature of such a population.

In this paper we attempt to derive a relationship between the observable electromagnetic (EM) emission and the predicted GW emission from AGN out to cosmological distances. In particular, we use the hard x-ray luminosity function of Ueda *et al.* [6] to infer the accretion history of supermassive black holes (SMBHs) out to redshifts of $z \sim 3$. Then we assume a few simple scaling factors, such as the average (Eddington-scaled) accretion rate and the efficiency of converting accretion energy to x rays, and derive the time-averaged GW spectrum that might be seen by LISA. Another important model parameter is the black hole spin, which will determine the radiative efficiency for gas accretion as well as the GW efficiency for inspirals. Based on relativistic MHD simulations of accretion disks [7–9], as well as some recent observations [10–12], there is growing evidence that most AGN black holes should be rapidly (but *not* maximally) spinning, with $a/M \simeq 0.9 - 0.95$. Observations of stellar mass black holes have yielded similar conclusions, with smaller spins of $a/M \simeq 0.7 - 0.8$ [13], consistent with the fact that these low-mass binary black holes do *not* gain most of their mass from accretion.

Depending on the specific model parameters, we find this background could be an important class of LISA sources, similar in strength and event rates to extreme mass-ratio inspirals (EMRIs) from captured compact objects [14]. As in those sources, here too it is a matter of preference as to whether the steady-state background should be thought of as signal or noise. But for higher masses (perhaps as large as $m \simeq 10^5 M_\odot$ [4]), provided such objects are not tidally disrupted before producing significant GW power, disk-embedded compact objects should produce individual, resolvable inspiral events with high signal-to-noise over a wide band of frequencies.

The outline of the paper is as follows: in Sec. II we give a brief overview of notation, and describe the cosmological x-ray luminosity distribution from AGN. In Sec. III we discuss the parameterization of the GW signal, from a single inspiral event to an integral of all sources over redshift and AGN luminosity. We then present the main results, showing the predicted GW power spectra for a range of model parameters and also for parameters that may depend on SMBH mass and redshift. In Sec. IV we estimate the expected event rates and duty cycle for LISA, which will be used to help distinguish between stochastic signals and resolvable ones. In Sec. V we discuss implications for the LISA mission as well as future GW observatories.

II. THE HARD X-RAY LUMINOSITY FUNCTION OF ACTIVE GALACTIC NUCLEI

We begin with a short discussion of notation. The results derived below include a number of dimensionless parameters, most of which can take values between 0 and 1. We divide these parameters into three general classes: efficiencies, fractions, and densities. Efficiencies, denoted by η, are believed to be determined by more basic physics, and typically have more stringent lower- and upper-limits. Fractions, denoted by f, are more model-dependent parameters and less-well known than the efficiency parameters, and thus have a larger range of acceptable values. Lastly, various cosmological density parameters Ω are given as fractions of the critical density $\rho_c \equiv 3H_0^2/(8\pi G)$. They are most likely constrained to very small values relative to unity. A summary of all the dimensionless parameters used in the paper appears in Table I, along with acceptable and preferred values.

The rest mass in supermassive black holes is estimated as $\Omega_{\rm SMBH} \simeq 2 \times 10^{-6}$, determined from galaxy surveys using the scaling relation between velocity dispersion and SMBH mass (the well-known "$M - \sigma$" relation; [10,15,16]). The energy density in the diffuse x-ray background between 2 keV and 10 keV is estimated as $\Omega_{\rm X} \simeq 2.6 \times 10^{-9}$ [17], to which AGN are believed to make a considerable contribution [6]. Now, assume that a fraction $f_{\rm acc} \leq 1$ of the SMBH rest mass density is due to accreted gas of cosmic density $\Omega_{\rm acc}$ (as opposed to mass gained through mergers), which releases electromagnetic radiation with an efficiency of $\eta_{\rm em} \leq 1$. We further assume that a fraction $f_{\rm X} \leq 1$ of the electromagnetic output is in the form of x rays in the range $2 - 10$ keV. This implies

$$f_{\rm acc}\Omega_{\rm SMBH} \simeq (1 - \eta_{\rm em})\Omega_{\rm acc} \tag{1}$$

and

$$\Omega_{\rm X} \simeq \langle \frac{1}{1+z} \rangle f_{\rm unobsc}\eta_{\rm X}\Omega_{\rm acc}, \tag{2}$$

where $\eta_{\rm X} \equiv f_{\rm X}\eta_{\rm em} \leq 1$, and the average inverse redshift of the sources $\langle (1+z)^{-1} \rangle \simeq 0.4$ is due to the redshifting of radiation energy. The parameter $f_{\rm unobsc}$ in the above equation is the fraction of the intrinsic x-ray luminosity that escapes the AGN region without obscuration or reprocessing. Since from observations $\Omega_{\rm X}/\Omega_{\rm SMBH} \simeq 1.3 \times 10^{-3}$, this gives the constraint

$$\langle \frac{1}{1+z} \rangle \frac{f_{\rm unobsc} f_{\rm acc} \eta_{\rm X}}{1 - \eta_{\rm em}} \simeq \frac{\Omega_{\rm X}}{\Omega_{\rm SMBH}} \simeq 1.3 \times 10^{-3}. \tag{3}$$

Since, for standard accretion disk theory $\eta_{\rm em} \lesssim 0.3$ [18], this immediately implies

$$f_{\rm unobsc} f_{\rm acc} f_{\rm X} \eta_{\rm em} \gtrsim 2 \times 10^{-3} \tag{4}$$

and thus

$$2 \times 10^{-3} \lesssim f_{\rm unobsc}, f_{\rm acc}, \eta_{\rm X}, f_{\rm X}, \eta_{\rm em} \lesssim 1. \tag{5}$$

The *lower limit* only depends on the fact that AGN contribute a considerable fraction of the observed x-ray background.

A growing consensus has been forming that SMBHs grow almost exclusively by accretion via a radiatively efficient mode of accretion [19], determined by linking luminosity distributions to the SMBH mass distribution,

TABLE I. Glossary of dimensionless parameters, with allowable and preferred values

Symbol	Min	Max	Preferred	Description
$f_{\rm acc}$	0	1	1	Fraction of SMBH mass due to accreted gas
$f_{\rm co}$	0	1	0.01	Fraction of accreted matter in form of compact objects
$f_{\rm X}$	0	1	0.03	Fraction of EM radiation in x rays
$f_{\rm Edd}$	0	$\gtrsim 1$	0.1	Typical fraction of Eddington luminosity/accretion rate
$f_{\rm unobsc}$	0	1	0.3	Fraction of emitted x rays not absorbed/reprocessed
$\eta_{\rm em}$	0	1	0.2	Accretion efficiency of converting gas to EM radiation
$\eta_{\rm X}$	0	$\eta_{\rm em}$	0.006	Accretion efficiency of converting gas to x rays
$\eta_{\rm gw}$	0	1	0.2	Accretion efficiency of converting compact objects to GW radiation
$\Omega_{\rm acc}$	0	$\Omega_{\rm SMBH}$	2×10^{-6}	Fraction of critical density in accreted gas
$\Omega_{\rm X}$	0	$\Omega_{\rm rad}$	2.6×10^{-9}	Fraction of critical density in x rays (2-10 keV)
$\Omega_{\rm SMBH}$	0	Ω_M	2×10^{-6}	Fraction of critical density in SMBHs
$\Omega_{\rm gw}$	0	$\Omega_{\rm SMBH}$	2×10^{-10}	Fraction of critical density in GWs
Ω_M	0	1	0.3	Fraction of critical density in matter
$\Omega_{\rm rad}$	0	1	5×10^{-5}	Fraction of critical density in radiation
Ω_Λ	0	1	0.7	Fraction of critical density in vaccuum energy

suggesting $f_{\rm acc} \simeq 1$. [10,11,15,20–23]. A corollary of this assumption is that most AGN should be rapidly spinning, with $\eta_{\rm em} \simeq 0.15 - 0.3$ for dimensionless spin parameters of $a/M \simeq 0.9 - 0.998$ [18]. As mentioned in the introduction, recent MHD simulations suggest an upper limit to the spin parameter, due to magnetic torques that remove angular momentum from the inner edge of the disk, thus preventing the accreted matter from spinning up the black hole to maximal spin [7–9]. Thus we set the fiducial spin parameter at $a/M = 0.95$, corresponding to $\eta_{\rm em} \simeq 0.2$.

For $f_{\rm unobsc} \simeq 0.3$ [6], Eq. (3) would then require an x-ray efficiency of accretion of $\eta_{\rm X} \simeq 7 \times 10^{-3}$. This would require either that the total radiative efficiency $\eta_{\rm em}$ would have to be of the same order, or that most of the electromagnetic emission is emitted in other bands. While such low radiative efficiencies are certainly possible (e.g., ADAF models of Ref. [24]), during the periods of largest growth and thus highest AGN activity, the accretion disks should be radiatively efficient. Indeed, the x-ray fraction $f_{\rm X}$ is governed by bolometric corrections and is of the order of 0.03 if AGN emission is dominated by infrared and optical frequencies [11,20,22,25]. This is consistent with the fact that the background energy in the x-ray band from 2 to 10 keV is dominated by AGNs, whereas the energy density in the infrared background which is about a factor 200 higher, is dominated by ordinary galaxies.

Pending a fuller understanding of the star formation mechanism in the accretion disk, for now we simply assume that a certain fraction $f_{\rm co} \leq 1$ of the accreted material is in the form of compact objects which will not get tidally disrupted before plunging into the SMBH. Since the astrophysical parameters that actually determine this fraction are not well known, we set it to a conservative value of 0.01. If it were much higher, the disk would be entirely fragmented and thus not efficiently emit EM radiation. And as we will see below, a value much below 1% would result in a GW signal undetectable by LISA. We further assume that a certain fraction $\eta_{\rm gw}$ of the rest mass m of these compact objects is emitted in GWs during the inspiral event. Neglecting the plunge and ringdown stages (as well as magnetic torques in the innermost disk), we will generally set $\eta_{\rm gw} = \eta_{\rm em}$.

Following the above notation, we now write the x-ray luminosity $L_{\rm X}$ as a fraction $f_{\rm X}$ of the bolometric luminosity, which in turn is a fraction $f_{\rm Edd}$ of the Eddington luminosity $L_{\rm Edd}$:

$$L_{\rm X} = f_{\rm X} f_{\rm Edd} L_{\rm Edd}(M) = f_{\rm X} \eta_{\rm em} \dot{M}_{\rm acc} c^2, \tag{6}$$

where the gas accretion rate is $\dot{M}_{\rm acc}$. The Eddington limit is a function only of the SMBH mass: $L_{\rm Edd}(M) = 1.3 \times 10^{38}(M/M_\odot)$ erg/s. Over the range of redshifts and luminosities we are probing, typical accretion rates during the period of maximum black hole growth are estimated to be $f_{\rm Edd} \sim 0.1 - 0.3$ [26], but could likely be even greater than unity [27–29]. This rate is also derived from a comparison of the luminosity distribution and the mass distribution, via the efficiency parameter $\eta_{\rm em}$. Note that Eq. (6), together with $f_{\rm X} \sim 0.03$ and $f_{\rm Edd} \sim 0.1$, implies that this luminosity function corresponds to SMBH masses $10^5 M_\odot \lesssim M \lesssim 10^{10} M_\odot$. This is consistent with typical SMBH masses inferred from velocity dispersion observations. Note, however, that $f_{\rm Edd}$ varies during the lifetime of an AGN and, strictly speaking, is a distribution for each SMBH mass and redshift. In the present work, we will understand $f_{\rm Edd}$ as an average during the active periods of AGNs, when they actually contribute to the x-ray luminosity function used below.

Emission in the infrared and hard x rays is less obscured than in other bands and are thus more easy to observe. Since infrared luminosity functions are more poorly known, we will use the x-ray luminosity function to obtain a realistic picture of AGN distributions. We stress that all our luminosities are to be understood as *intrinsic*, i.e. as a measure of the x rays produced directly by the accreting gas, and before reprocessing and/or partial absorption within the host galaxy [6,22]. This is most natural for our purposes as we are dealing with electromagnetic and GW emission by accretion, so we are concerned primarily with emission from the very inner-most regions of the disk.

The luminosity function is defined as the comoving number density n of objects per logarithmic luminosity interval, with units of Mpc^{-3}. We parametrize the intrinsic x-ray luminosity function per comoving volume after Ref. [6],

$$L_{\rm X}\frac{dn}{dL_{\rm X}}(z, L_{\rm X}) = \frac{A}{(\frac{L_{\rm X}}{L_*})^{\gamma_1} + (\frac{L_{\rm X}}{L_*})^{\gamma_2}} \times \begin{cases} (1+z)^{p_1} & z < z_c(L_{\rm X}), \\ \frac{(1+z)^{p_2}}{[1+z_c(L_{\rm X})]^{p_2-p_2}} & z \geq z_c(L_{\rm X}), \end{cases} \tag{7}$$

for $L_{\rm min} \simeq 10^{41.5}{\rm ergss}^{-1} \leq L_{\rm X} \leq 10^{46.5}{\rm ergss}^{-1} \simeq L_{\rm max}$. For a given $L_{\rm X}$, the cutoff redshift is

$$z_c(L_{\rm X}) = \begin{cases} z_c^* & L_{\rm X} \geq L_a \\ z_c^*\left(\frac{L_{\rm X}}{L_a}\right)^\beta & L_{\rm X} < L_a \end{cases}, \tag{8}$$

and the best fit parameters in Eqs. (7) and (8) are given by $A = 2.2 \times 10^{-6}{\rm Mpc}^{-3}$, $L_* = 10^{44}{\rm ergss}^{-1}$, $\gamma_1 = 0.86$, $\gamma_2 = 2.23$, $p_1 = 4.23$, $p_2 = -1.5$, $z_c^* = 1.9$, $L_a = 10^{44.6}{\rm ergss}^{-1}$, and $\beta = 0.335$ (note that our value for the parameter A differs from Ref. [6] by a factor of (ln10) due to our slightly different definitions of the luminosity function). The distribution function defined by Eq. (7) is plotted in Fig. 1 for a range of redshifts. The "antihierarchical growth" of AGN is evident from the increasing average luminosity with redshift: at early times, *larger* black holes were growing fastest, and most smaller black holes ($M \sim 10^6 - 10^7 M_\odot$) are thus relatively young [22,23].

With this luminosity function, we can calculate directly the diffuse energy density in hard x rays due to AGN:

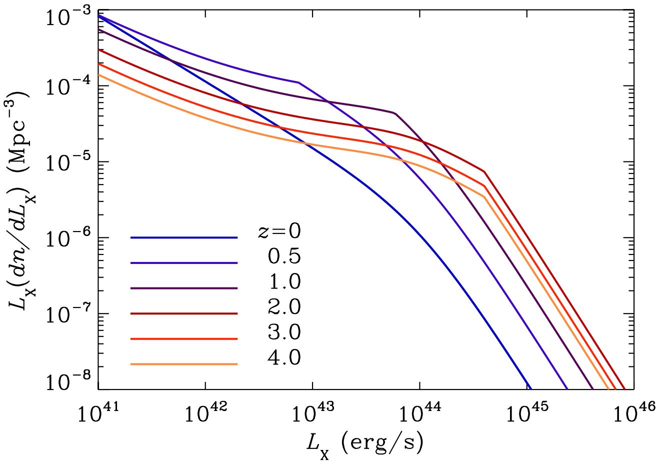

FIG. 1 (color online). Analytic fits to the hard x-ray luminosity function given in Ref. [6]. Note that the average intrinsic luminosity (and thus AGN mass) increases with redshift.

$$\rho_c \Omega_{\rm X} \simeq f_{\rm unobsc} \int_0^\infty dz \left| \frac{dt}{dz} \right| \frac{1}{1+z} \int dL_{\rm X} L_{\rm X} \frac{dn}{dL_{\rm X}}. \qquad (9)$$

In Eq. (9), cosmology enters through $|dt/dz| = [(1+z)H(z)]^{-1}$ and, for a flat geometry,

$$H(z) = H_0[\Omega_{\rm M}(1+z)^3 + \Omega_\Lambda]^{1/2}. \qquad (10)$$

Throughout this paper we will assume a flat, ΛCDM Universe with $\Omega_{\rm M} = 0.3$, $\Omega_\Lambda = 0.7$ (all other contributions to the energy density are negligible), and $H_0 = 72{\rm kms}^{-1}{\rm Mpc}^{-1}$ [30]. Typically, we will integrate the luminosity function out to redshifts $z_{\rm max} \simeq 3$.

Reference [6] has demonstrated that, when integrated over redshift and correcting for absorption and reprocessing, the luminosity function (7) explains practically all of the diffuse extra-galactic x-ray flux between $\simeq 1$ keV and a few hundred keV measured by the HEAO1, ASCA, and Chandra observatories. Combining Eqs. (7) and Eq. (9), we obtain $\Omega_{\rm X} \simeq 8.7 \times 10^{-9} f_{\rm unobsc}$, implying $f_{\rm unobsc} \simeq 0.3$. This is consistent with the estimate that about 60% of AGNs of luminosity $L_{\rm X} \lesssim 10^{44}$ ergss^{-1} are obscured [22]. The unobscured fraction of these AGN dominates Ω_X.

More information may come from future x-ray missions such as Astro-E2/HXD, EXIST, NeXT, Constellation-X, and XEUS. With their larger collecting area and greater sensitivity, these instruments will allow us to extend the x-ray luminosity function to lower luminosities and higher redshifts. Future IR observatories like the James Webb Space Telescope will greatly improve our estimates for $f_{\rm X}$ and $f_{\rm unobsc}$. There may also be significant AGN emission in soft $\gamma-$rays, as recently reported from INTEGRAL observations [31]. Future $\gamma-$ray missions such as GLAST will further help us understand the AGN energy budget at this end of the spectrum.

The density of AGNs contributing to the luminosity function Eq. (7) is given by

$$\Omega^{\rm X}_{\rm SMBH} \sim \int dL_X (dn/dL_X) M/\rho_c, \qquad (11)$$

where M is related to L_X via Eq. (6). For the fiducial parameters given in Table I, we have $\Omega^{\rm X}_{\rm SMBH} \simeq 1.5 \times 10^{-8}$. Comparing with $\Omega_{\rm SMBH} \simeq 2 \times 10^{-6}$, this suggests that AGNs have a duty cycle of $\sim$1%, or $\sim 10^7$yr today, which is consistent with comparing the number of quasars and galaxies [32].

III. THE GRAVITATIONAL-WAVE SIGNAL

A. Individual inspiral spectrum

We consider the inspiral of a single compact object of mass m into a SMBH of mass $M \gg m$, motivated by scenarios such as those described in the introduction [4,5]. It is not known whether inspiraling black holes in accreting discs can acquire considerable eccentricity by interacting with the disc or with other orbiting masses, and if this eccentricity will have time to decrease due to GW radiation reaction as the small body spirals in. If the accretion disk does not strongly modify the final inspiral phase dominated by GW emission, the orbits should circularize sufficiently that the emitted GW power is only modified at frequencies much smaller than the ones relevant for LISA [33]. Considering the astrophysical uncertainties in deriving the GW spectrum, we limit the analysis to the simplest inspiraling model, i.e. the circular equatorial one.

We note that a main sequence star would be tidally disrupted before reaching the inner-most stable circular orbit (ISCO) if $M \lesssim 10^8 M_\odot$, thus modifying the GW signal compared to our estimation. This, however, is not the case for neutron stars or black holes. Even white dwarfs should survive the tidal disruption forces up to the ISCO of any black hole with mass greater than $\sim 5 \times 10^5 M_\odot$ [34].

We also assume that interactions between the compact objects and the accretion disk do not significantly change the gravitational-wave signal. Inspiral is driven by the rate of change of the angular momentum of the compact object. At early stages of inspiral it is driven mostly by viscous drag, whose time scale for main sequence stars is very roughly $t_{\rm hd} \sim 1.8 \times 10^8 (M/10^6 M_\odot)(r_{\rm form}/10^4)^2 \times (m/10M_\odot)^{-1}(f_{\rm Edd}/0.1)^{-1}$ yr, where $r_{\rm form}$ is the radius (in gravitational radii GM) in the disk at which the star is formed [35]. This provides more than enough time for any main sequence star with initial mass $\gtrsim 10 M_\odot$ to evolve into a compact object (the typical time to evolve to a compact object being $\lesssim 10^7$ years). At the latest stages it is dominated by GW emission whose time scale is roughly estimated by Eq. (31) below. Comparing these timescales shows that at the frequencies relevant for LISA, $f \gtrsim 10^{-4}$ Hz, hydrodynamic effects are basically negligible, as least as long as one is not interested in detailed templates. Furthermore, the importance of nongravitational effects decreases with increasing compactness of the inspiraling object and with decreasing accretion rate [35,36], especially in the later stages of the stars evolution, when a gap has likely been created in the accretion disk [4].

Using geometrized units such that $G = c = 1$, a geodesic particle on an equatorial, circular orbit around a Kerr black hole has an orbital frequency (as measured by an observer at infinity) of [37]

$$f_{\rm orb}(r) = \frac{\sqrt{M}}{2\pi(r^{3/2} \pm a\sqrt{M})} \tag{12}$$

and specific energy

$$\frac{E(r)}{m} = \frac{r^2 - 2Mr \pm a\sqrt{Mr}}{r(r^2 - 3Mr \pm 2a\sqrt{Mr})^{1/2}}. \tag{13}$$

We estimate the total energy emitted in gravitational waves down to a radius r as $E_{\rm gw}(r) = m - E(r)$. The energy emitted in GWs between frequency f and $f + df$ for such an event is

$$\frac{dE_{\rm gw}}{df} = \frac{dE_{\rm gw}}{dr}\left(\frac{df}{dr}\right)^{-1}. \tag{14}$$

We restrict the GW emission to the leading quadrupole formula, thus we consider only GW frequencies twice the orbital frequencies. In the Newtonian limit, we reproduce the well-known result (e.g. Refs. [38,39]) valid for circular orbits

$$f\frac{dE_{\rm gw}}{df}(f) = \frac{m}{3}(\pi M f)^{2/3}. \tag{15}$$

We will generally want to restrict Eq. (14) to a range of frequencies $f_{\rm min} \le f \le f_{\rm max}$. Here, $f_{\rm min} \equiv T_{\rm obs}^{-1}$ is the smallest resolution frequency-bin determined by the mission lifetime $T_{\rm obs}$ and $f_{\rm max}$ is the GW frequency at the ISCO. The location of the ISCO is given by the radius where $dE_{\rm gw}/df$ in Eq. (14) vanishes. It strongly depends on the spin of the black hole, giving $f_{\rm max} \simeq 4 - 20$ mHz for a SMBH mass $10^6 M_\odot$ [37]. Note that $\eta_{\rm gw} = \int_0^{f_{\rm max}} df(dE_{\rm gw}/df)/m$ is given by Eq. (14).

In Fig. 2 we show the GW spectrum for a single inspiral event for a range of black hole masses and spins, plotting the so-called *characteristic* GW amplitude $h_c(f)$ for single events, defined by

$$h_c^2(f) = \frac{2}{\pi^2}\frac{1}{r^2(z)}\frac{dE_{\rm gw}}{df}(f_z) \tag{16}$$

(compare with Figs. 3–7 in Ref. [40]), where $r(t)$ is the comoving coordinate, $dr = (1 + z)dt$.

We note that for all the calculations presented in this paper, we neglect GW emission during the plunge and ringdown phases of the merger. Whereas the inclusion of plunge and ringdown phases would increase the signal-to-noise (SNR) for supermassive black holes binaries of comparable masses, it would not increase the SNR very much for the extreme mass-ratio binaries investigated in this paper. In fact, in the latter case the GW energy in the inspiral up to the ISCO is proportional to m, and the energy in the ringdown portion scales as $m(m/M)$ [41].

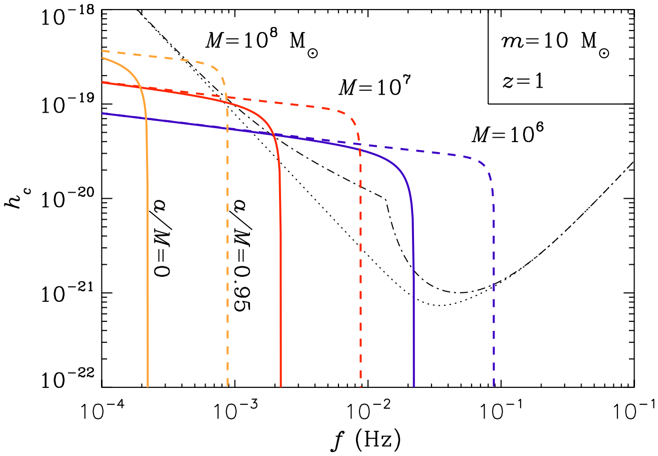

FIG. 2 (color online). Characteristic GW strain amplitudes for individual inspiral events, where a black hole with $m = 10M_\odot$ merges with a SMBH of mass $M = 10^6, 10^7, 10^8 M_\odot$ at a redshift of $z = 1$. For each value of M, we show the spectra for two spin values, $a/M = 0$ (solid) and 0.95 (dashed). The dashed-dotted and dotted lines are the sky-averaged LISA noise curves with and without the contributions from galactic binaries, respectively.

B. Integrated time-averaged spectrum

To estimate the total contribution from all sources, we start by integrating the GW energy density (per logarithmic frequency) over redshift z, averaged over time scales large compared to all physical time scales related to the sources. Following Ref. [39], we have

$$\frac{d\rho_{\rm gw}(f)}{d\ln f} = \int_0^\infty dz\frac{R(z)}{1+z}\left|\frac{dt}{dz}\right| f_z\frac{dE_{\rm gw}}{df_z}(f_z), \tag{17}$$

where $f_z \equiv (1 + z)f$, and $R(z)$ is the rate of inspiral events per comoving volume. Note the similarity to Eq. (9), the energy density in hard x rays.

To derive an expression for $R(z)$, we observe that the event rate for a single AGN is simply the x-ray luminosity divided by the total x-ray energy emitted between inspiral events and thus for a given luminosity $L_{\rm X}$, the event rate is

$$R(L_{\rm X}, z) = \frac{dn}{dL_{\rm X}}\frac{L_{\rm X}}{E_{\rm X}}. \tag{18}$$

Assuming equal efficiencies $\eta_{\rm gw} = \eta_{\rm em}$, this x-ray energy can be written as

$$E_{\rm X} = E_{\rm gw}\frac{f_{\rm X}}{f_{\rm co}}. \tag{19}$$

Combining Eqs. (18) and (19) and integrating over the luminosity distribution function, we get

$$R(z) = \frac{f_{\rm co}}{f_{\rm X}} \int dL_{\rm X} \frac{dn}{d\ln L_{\rm X}} \frac{1}{E_{\rm gw}}. \tag{20}$$

Combining with Eq. (17) and integrating over redshift, the total (time-averaged) gravitational-wave spectrum is

$$\frac{d\rho_{\rm gw}(f)}{d\ln f} = \frac{f_{\rm co}}{f_X} \int_0^\infty \left|\frac{dt}{dz}\right| \frac{dz}{1+z} \times \int_{L_{\rm min}}^{L_{\rm max}} dL_{\rm X} \frac{dn}{d\ln L_{\rm X}} \frac{1}{E_{\rm gw}} \frac{dE_{\rm gw}}{d\ln f_z}(f_z). \tag{21}$$

The GW spectrum $E_{\rm gw}(f)$ from each individual AGN is a function of the SMBH mass, which in turn is determined by the x-ray luminosity through Eq. (6). Note that the integrated spectrum is independent of m, as long as m is small enough so that the inspiral waveforms cannot be individually resolved. One measure of this resolvability is the *duty cycle*, described in the next section.

Following Refs. [14,40], we will want to compare directly the stochastic background defined in Eq. (21) to the spectral density of the detector noise $S_{\rm n}(f)$, which has units of inverse frequency. In this case, $\sqrt{fS_{\rm n}(f)}$ will have units of dimensionless strain. Averaging over the entire sky, weighted by the LISA antenna pattern, gives

$$S_h(f) = \frac{4}{\pi} \frac{1}{f^3} \frac{d\rho^{\rm av}_{\rm gw}(f)}{d\ln f}. \tag{22}$$

Throughout the paper we use the so-called sky and detector averaged instrumental spectral density for LISA, given by [14,40]:

$$S^{\rm instr}(f) = \left[6.12 \times 10^{-51}\left(\frac{f}{1{\rm Hz}}\right)^{-4} + 1.06 \times 10^{-40} + 6.12 \times 10^{-37}\left(\frac{f}{1{\rm Hz}}\right)^{2}\right]{\rm Hz}^{-1}, \tag{23}$$

augmented by the white-dwarf galactic confusion noise

$$S_h^{\rm gal}(f) = 1.4 \times 10^{-44}\left(\frac{f}{1{\rm Hz}}\right)^{-7/3} {\rm Hz}^{-1}, \tag{24}$$

and the white dwarfs extra-galactic confusion noise

$$S_h^{\rm ex-gal}(f) = 2.8 \times 10^{-46}\left(\frac{f}{1{\rm Hz}}\right)^{-7/3} {\rm Hz}^{-1}. \tag{25}$$

Thus, the total (instrumental plus confusion) noise is

$$S_{\rm n}(f) = \min\{S^{\rm instr}(f)/\exp(-\kappa T^{-1}_{\rm mission} dN/df), S_h^{\rm instr}(f) + S_h^{\rm gal}(f)\} + S_h^{\rm ex-gal}(f). \tag{26}$$

Here, dN/df is the number density of galactic white-dwarf binaries per unit gravitational-wave frequency given by

$$\frac{dN}{df} = 2 \times 10^{-3}{\rm Hz}^{-1}\left(\frac{1\ {\rm Hz}}{f}\right)^{11/3}. \tag{27}$$

C. Dependence on model parameters

In this section we show the impact of each of the model parameters on the predicted GW spectrum. In this approach, all parameters are taken as constant in time and independent of the other parameters and the AGN masses. In Fig. 3, we show the time-averaged GW spectrum calculated from Eq. (21), for the fiducial model parameters listed in Table I (solid black curves), along with the effects of varying the individual parameters around these baseline values.

In the top left panel of Fig. 3 we show the dependence on $f_{\rm Edd}$ relative to the fiducial model. For smaller values of $f_{\rm Edd}$, the observed luminosity function will imply a SMBH mass distribution function shifted towards higher masses and thus lower frequencies (blue curve). Conversely, higher values of $f_{\rm Edd}$ require smaller black hole masses and thus higher frequencies (red curve).

The top right panel of Fig. 3 shows the dependence on $f_{\rm co}$, the fraction of accreted matter in the form of compact objects. The linear dependence of $\Omega_{\rm gw}(f)$ on $f_{\rm co}$ is reasonable: more compact objects give more signal, which is also clear from Eq. (21). Similarly, the predicted GW power increases when the fraction $f_{\rm X}$ *decreases*, as seen in the bottom left panel of Fig. 3. The largest GW signal in this scenario is achieved for minimal $f_{\rm X}$. This corresponds to only a small fraction of the total accretion activity in the Universe being observable in hard x rays. Thus we infer that the bolometric luminosities are actually much higher, which in turn implies more matter being accreted and thus more compact objects for a fixed $f_{\rm co}$. The fraction $f_{\rm X}$ also determines the AGN mass cutoff through Eq. (6), since (fixing all other parameters) a smaller $f_{\rm X}$ implies a larger Eddington luminosity, and thus higher mass and lower frequency.

Motivated by Refs. [8,9], we have used a large (yet not maximal) spin parameter of $a/M = 0.95$ for most of the calculations here. The bottom right panel of Fig. 3 shows the fiducial model along with the corresponding signal for $a/M = 0$, 0.7, and 1.0. Despite the significant difference between the signals from individual inspiral events (see Fig. 2), the difference in total, time-averaged power is rather smaller. This is because rapidly spinning black holes are more efficient (high $\eta_{\rm em}$ and $\eta_{\rm gw}$), so for a given luminosity, there is less gas being accreted and therefore fewer embedded compact objects, and less GW power. Similar to the results in the bottom left panel of Fig. 3, varying a/M also changes the inferred SMBH mass for a given luminosity, in turn changing the cutoff frequency.

We should mention that the GW signal appears to depend insignificantly on the maximal redshift $z_{\rm max}$ for $z_{\rm max} \gtrsim 3$, where the luminosity function becomes more and more uncertain. Another parameter that we have explored is the low-luminosity cutoff of the luminosity function Eq. (7). By extending the cutoff to lower luminosities, we include lower-mass AGN, and thus higher frequencies.

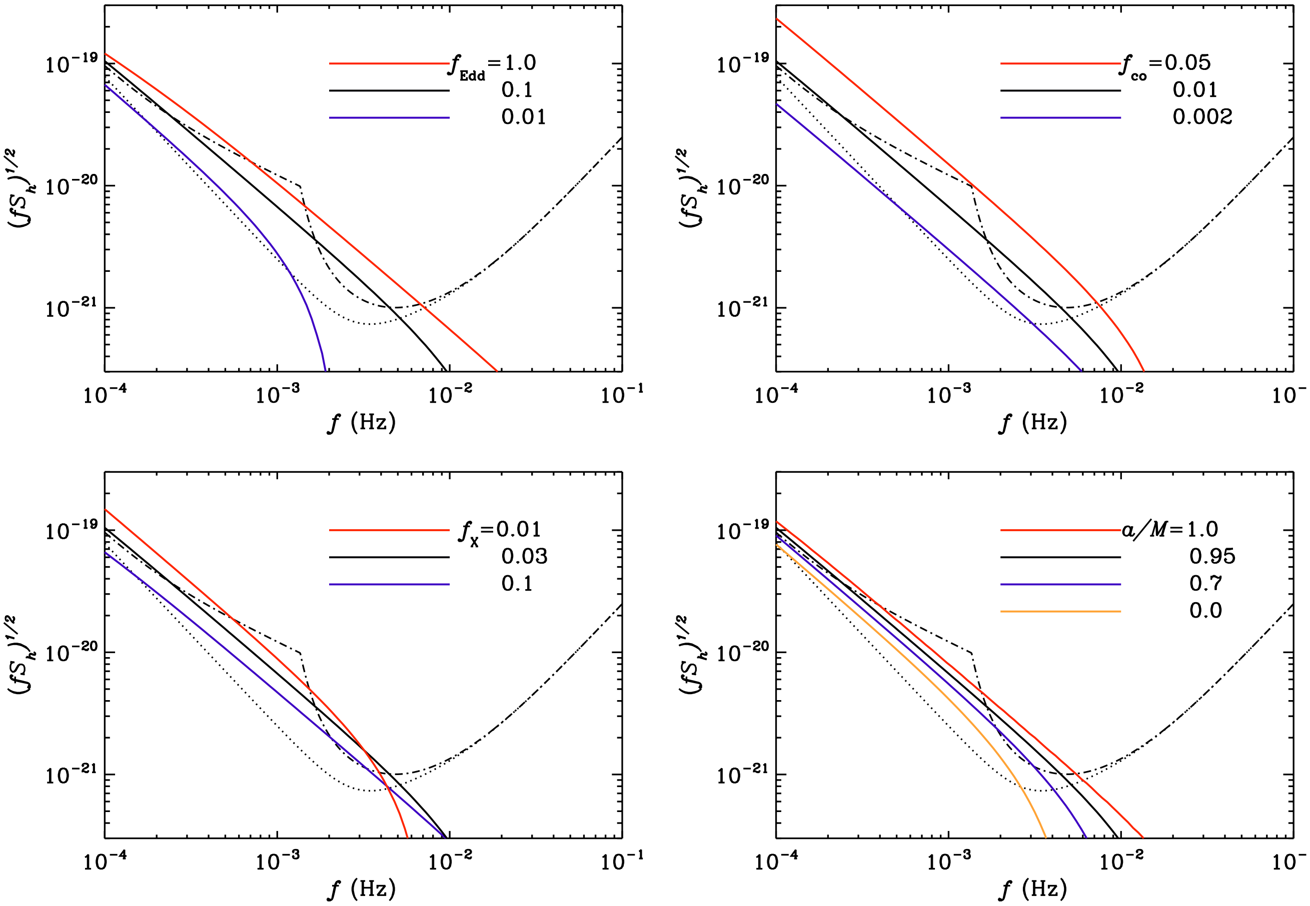

FIG. 3 (color online). Time-averaged GW spectra for the baseline model parameters listed in Table I (solid black curves), and the effects of changing the various parameters: $f_{\rm Edd}$ (top left panel), $f_{\rm co}$ (top right), $f_{\rm X}$ (bottom left), and a/M (bottom right). The dashed-dotted and dotted lines are the sky-averaged LISA noise curves with and without the contributions from galactic binaries, respectively.

After trying $L_{\rm min} = 10^{40.5}$ ergs s^{-1} and $L_{\rm min} = 10^{39.5}$ ergs s^{-1} we found that, as expected, the lower luminosities give more signal at higher frequencies, but not significantly within the LISA band. However, this may be an important factor when designing a GW observatory with more sensitivity in the $\sim 0.1 - 10$ Hz band. On the other hand, the smaller accretion disks and shorter time scales of low-mass AGN may make them insignificant sources of disk-embedded compact objects, and thus the somewhat artificial cutoff of $L_{\rm min} = 10^{41.5}$ ergs s^{-1} may actually be physically justified.

D. Sensitivity to varying model parameters

Up to now we have assumed that the fiducial values of the parameters in Table I are constants independent of SMBH mass and/or redshift. Particular parameters are, however, likely to vary throughout evolution. There is evidence, for example, that the Eddington ratio $f_{\rm Edd}$ was higher in the past than it is now, see, e.g., Refs. [25,42]. In order to assess the possible influence of such evolution, following Ref. [42] who studied an AGN sample from the Sloan Digital Sky Survey, we model the dependence of the average $f_{\rm Edd}$ on the SMBH mass and redshift as follows (while restricting $0.01 \le f_{\rm Edd} \le 1.0$):

$$f_{\rm Edd}(M, z) = 0.1\left(\frac{z}{0.1}\right)^{\gamma(M)}\left(\frac{M}{10^7 M_\odot}\right)^{-0.8}, \qquad (28)$$

where $\gamma(M)$ is given by Eq. (4), Table 1, and Fig. 4 in Ref. [42]. This may in fact be more realistic than the constant $f_{\rm Edd} \simeq 0.1$ approximation, because it takes into account the dominance of low-luminosity AGNs at low redshifts: For $z \sim 0.01$, the SMBH density resulting from the x-ray luminosity function, $\Omega^{\rm X}_{\rm SMBH} \simeq 1.3 \times 10^{-6}$ is closer to the one inferred from the velocity dispersions in the AGNs. This results from Eqs. (11) where M is related to L_X via the generalization of Eq. (6) to varying $f_{\rm Edd}$, $L_X = f_X f_{\rm Edd}(M, z) L_{\rm Edd}(M)$, and M is restricted to $10^5 M_\odot \lesssim M \lesssim 10^{10} M_\odot$. The time-averaged GW spectrum resulting from Eq. (28) is shown in the left panel of Fig. 4. Compared to the fiducial model (black curve), when varying $f_{\rm Edd}$ (red curve), the slope becomes smaller, i.e. the signal at low-frequency decreases whereas at high frequencies it increases, consistent with the tendencies seen in the top left panel of Fig. 3. Overall, the spectrum seems relatively robust with respect to variation of $f_{\rm Edd}$.

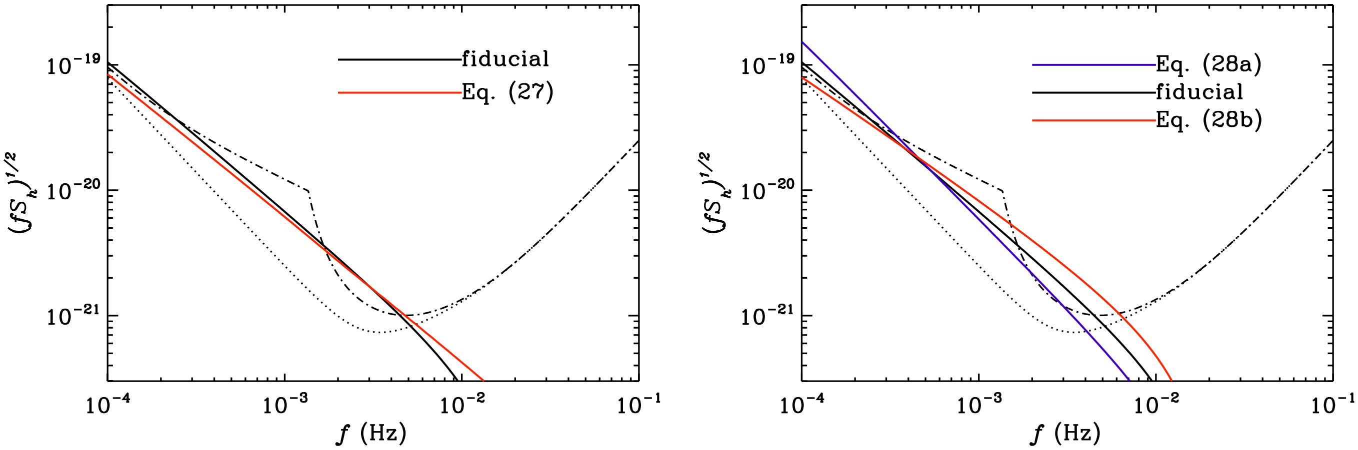

FIG. 4 (color online). Time-averaged GW spectra for the baseline model parameters listed in Table I (solid black curves), along with models where $f_{\rm Edd}$ varies according to Eq. (28) (left panel, red curve) or the fraction $f_{\rm co}$ of accreted matter in form of compact objects varies according to Eq. (29) (right panel, red, and blue curves).

Furthermore, since the larger mass disks seem more susceptible to fragmentation into smaller mass objects, $f_{\rm co}$ might increase with M, whereas m might decrease with M. For large M, the longer accretion times also make it more likely for lower-mass stars to form and evolve to compact objects before reaching the inner edge of the disk. On the other hand, the feedback into the disk from star formation may increase gravitational stability and thus decrease $f_{\rm co}$. For purpose of illustration we consider each of the following scalings:

$$f_{\rm co}(M) = 10^{-3}\left(\frac{M}{10^5 M_\odot}\right)^{0.5} \quad \text{and} \tag{29a}$$

$$f_{\rm co}(M) = 10^{-3}\left(\frac{10^9 M_\odot}{M}\right)^{0.5}, \tag{29b}$$

in all cases requiring $f_{\rm co} \lesssim 0.5$ to maintain a coherent gas accretion disk in order to produce the necessary x-ray flux. The resulting time-averaged GW spectrum is shown in the right panel of Fig. 4. When $f_{\rm co}$ increases with M, the signal is considerably enhanced at low frequencies (blue curve), while the opposite occurs when $f_{\rm co}$ decreases with M (red curve).

IV. EVENT RATES, DUTY CYCLE AND CONFUSION NOISE

The total inspiral rate as seen from Earth at frequency f can be written as (see, e.g. Ref. [39])

$$\begin{aligned}\Gamma(f) &= \int_0^\infty dz \frac{R(z)}{1+z}\frac{dV}{dz} \\ &= \frac{f_{\rm co}}{f_{\rm X}\eta_{\rm em} m}\int_0^\infty dz \frac{4\pi r^2(z)}{(1+z)H(z)} \\ &\quad \times \int_{L_{\rm min}}^{L_{\rm max}(f_z)} dL_{\rm X}\frac{dn}{d\ln L_{\rm X}},\end{aligned} \tag{30}$$

where $dV/dz = 4\pi r^2(z)/H(z)$ is the fractional volume element, the Hubble rate at redshift z is given by Eq. (10), and $r(z)$ is the comoving coordinate, $dr = (1+z)dt$. In the second expression of Eq. (30) we have used Eq. (20) with $E_{\rm gw} = \eta_{\rm gw} m$ and $L_{\rm max}(f)$ is the maximum luminosity for which the associated SMBH mass emits to frequencies up to f. Note that for a fixed compact object fraction $f_{\rm co}$, the rate Eq. (30) is inversely proportional to the typical mass m of the inspiraling compact object.

The *duty cycle* $\mathcal{D}(f)$ at a given frequency is the average number of sources contributing at any given time. This can be estimated by multiplying the integrand of Eq. (30) with the time scale over which a source radiates around the frequency f with a coherent phase development. In the case of adiabatic, circular inspirals, the system emits GWs at a well-defined frequency $f(t)$ which evolves monotonically in time. In the local rest frame (i.e. ignoring cosmological redshifts) we can estimate the coherence time as [43]:

$$\begin{aligned}t_{\rm coh}(f) &\equiv \frac{f}{df/dt} \simeq \frac{5}{144 M^{2/3} m (\pi f)^{8/3}} \\ &\simeq 3.5\left(\frac{10^6 M_\odot}{M}\right)^{2/3}\left(\frac{10^2 M_\odot}{m}\right)\left(\frac{10^{-3}\,{\rm Hz}}{f}\right)^{8/3} {\rm yr}.\end{aligned} \tag{31}$$

The duty cycle as observed at Earth will thus be estimated by multiplying the integrand of Eq. (30) with $(1+z)t_{\rm coh}(f_z)$:

$$\mathcal{D}(f) = \frac{f_{\rm co}}{f_{\rm X}\eta_{\rm em} m}\int_0^\infty \frac{4\pi r^2(z)}{H(z)}dz \int dL_{\rm X}\frac{dn}{d\ln L_{\rm X}} t_{\rm coh}(f_z). \tag{32}$$

Note that it is proportional to $f_{\rm co}/(f_{\rm X}\eta_{\rm em} m^2)$, with the extra power of m coming from the dependence of $t_{\rm coh}$ in Eq. (31). Smaller m means more compact objects, and also

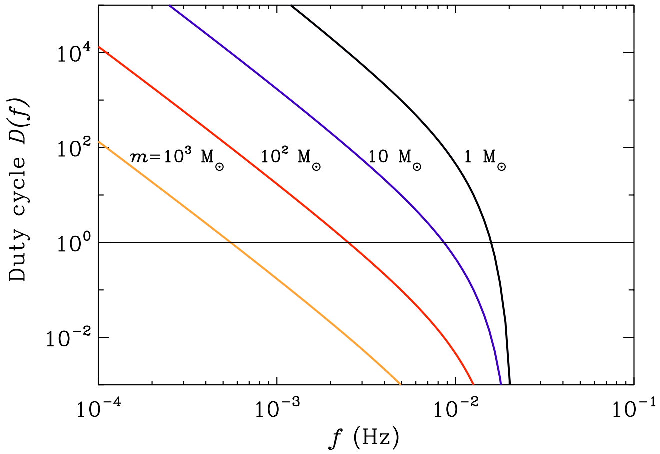

FIG. 5 (color online). Duty cycle $\mathcal{D}(f)$ for the nominal parameter values and a range of compact object masses m. When $\mathcal{D}(f) \lesssim 1$, the inspiral signals could be individually resolvable. The high frequency cutoff is due to the somewhat arbitrary cutoff of the x-ray luminosity function at low luminosities which depends on the experimental sensitivity.

slower inspiral rates, thus each source spends more time around a given f.

In Fig. 5 we show the duty cycle for the fiducial model parameters and a range of compact object masses m. The cutoff around 20 mHz is due to the somewhat artificial low-end cutoff in the luminosity function, corresponding to a minimum value for M and thus maximum attainable frequency. When the duty cycle is $\lesssim 1$, a detector will see a non-Gaussian, noncontinuous signal which rather has a "popcorn" character [44]. Provided the SNR is sufficiently large, the detector will then be able to resolve individual events of duration $t_{\rm coh}(f)$, occurring at a rate $\Gamma(f) < t_{\rm coh}^{-1}(f)$.

When the duty cycle is $\gtrsim 1$, several sources are present at any given time at a frequency f in a bandwidth $\Delta f \sim f$. However, the number of sources in the smallest resolution frequency-bin, which corresponds to $1/T_{\rm obs} \sim 10^{-8}$ Hz, is not larger than 1. Thus, our background is in principle subtractable if the SNR is sufficiently high.

Let us estimate, as done in Ref. [14], the unsubtractable portion which will constitute the *confusion* noise $S^{\rm conf}(f)$ [or $d\rho_{\rm gw}^{\rm conf}(f)/df$ related to $S_h^{\rm conf}(f)$ by the analogue of Eq. (22)]. For each inspiral source observed over the LISA mission lifetime, we evaluate the SNR defined by

$$\mathrm{SNR}^2 = \int_{f_{\rm min}}^{f_{\rm max}} d\ln f \, \frac{h_c^2(f)}{f S_{\rm n}}, \tag{33}$$

where $h_c(f)$ is the characteristic strain defined in Eq. (16) and $S_{\rm n}$ is given by Eq. (26). This integral is performed over the frequency range $f_{\rm min} \leq f \leq f_{\rm max}$ through which the system sweeps during the mission lifetime $T_{\rm obs}$. While in principle the inspiraling object may reach $f_{\rm ISCO}$ and then plunge sometime in the middle of the LISA mission, for concreteness we only consider systems that are active throughout $T_{\rm obs}$. In Fig. 6 we show SNRs for a few typical cases as a function of the time t remaining to plunge (as of the end of the observation). We then insert a step-function factor $\Theta(\mathrm{SNR}_{\rm thr} - \mathrm{SNR})$ in the integrand of Eq. (21) to obtain $d\rho_{\rm gw}^{\rm conf}(f)/df$. This assures that only events with SNR too small to be subtracted out contribute to this confusion noise.

We note in passing that, strictly speaking, unresolvable events contribute to the $S_{\rm n}$ noise and thus the SNR in Eq. (33) should be obtained by an iterative procedure in which $S_{\rm n}$ includes events that could not be subtracted out. This becomes important when the merger noise of events whose SNR is smaller than the threshold SNR is comparable or larger than the instrumental noise. In this case we will slightly underestimate the fraction of the true unsubtractable background.

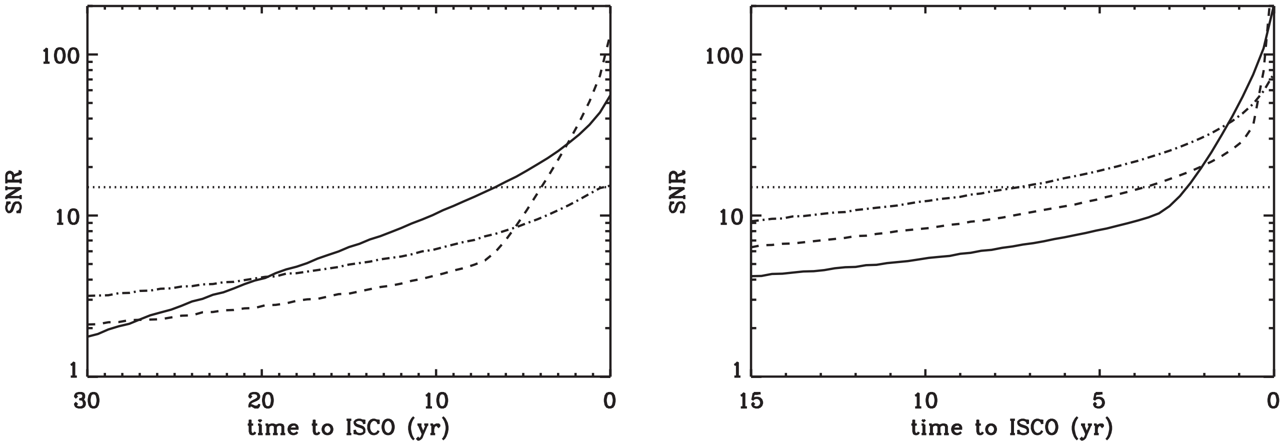

FIG. 6. Signal-to-noise ratio for the inspiral of a compact object of masses (left panel) $10M_\odot$ and (right panel) $100M_\odot$ onto a SMBH of mass $M = 10^5 M_\odot$ (solid line), $M = 10^6 M_\odot$ (dashed line), and $M = 10^7 M_\odot$ (dashed-dotted line) at 1 Gpc distance, as a function of the time left to the ISCO at the end of the observation time $T_{\rm obs} = 3$ yr. Also shown is the threshold of SNR=15 (dotted line).

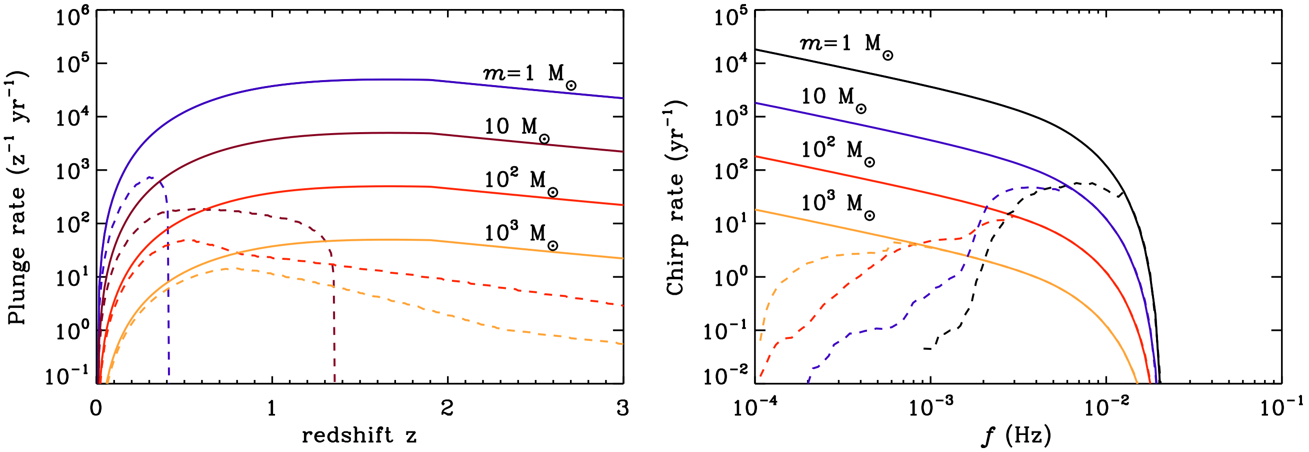

FIG. 7 (color online). In the left panel we show the inspiral rate $\Gamma(z)$ as a function of redshift for $m = 1 - 10^3 M_\odot$. The solid curves represent the total plunging rate in the Universe irrespective of frequency, while the dashed curves represent the resolvable fraction with maximal SNR ≥ 15 In the right panel we show the total inspiral chirp rate $\Gamma(f)$ of Eq. (30) for the same range of masses, again distinguishing between the total rate in the Univers (solid curve) and the resolvable portion (dashed curves).

With the SNR calculation in hand, we can also estimate the inspiral rate above a given threshold. In the left panel of Fig. 7, we show both the total inspiral rate in the Universe (solid curves), as well as the rate of detectable signals for SNR ≥ 15 (dashed curves), for $m = 1 - 10^3 M_\odot$. The total rate, which here can be thought of as the rate of compact objects reaching the ISCO, is given at each redshift as

$$\Gamma(z) = \frac{R(z)}{1+z} \frac{dV}{dz}. \tag{34}$$

We have also defined [see Eq. (30)] an inspiral rate as a function of frequency $\Gamma(f)$, which is a measure of the number of chirping systems that passes through a frequency f per unit time. To distinguish these rates, we will refer to $\Gamma(z)$ as the "plunge rate" and $\Gamma(f)$ as the "chirp rate."

While the plunge rate is proportional to m^{-1}, the SNR increases with m, so the smaller mass inspirals are only resolvable out to smaller distances. Also, at a given redshift, the integrated SNR generally decreases with increasing M as the lower $f_{\rm ISCO}$ resides in the region of higher instrumental noise. By integrating the area under the dashed curves in Fig. 7, we find the resolvable event rates to be $\sim 150\ {\rm yr}^{-1}$ for $m = 1 - 10 M_\odot$ and $\sim 50\ {\rm yr}^{-1}$ for $m = 100 M_\odot$. Inspirals with $m = 10^3 M_\odot$, while observable out to high redshifts, would be relatively rare, with rates $\sim 15\ {\rm yr}^{-1}$. From Eq. (30), we see that these plunge rates are proportional to $f_{\rm co}$, so could potentially be used to constrain that poorly-known parameter.

In the right panel of Fig. 7 we plot the chirp rate $\Gamma(f)$ for the same range of compact object masses. At low frequencies, the chirp rate funtion is nearly flat, due to a steady-state "flux conservation" as each inspiraling object enters a frequency bin, another will leave it. Then, at higher frequencies, systems begin to drop out altogether as they reach the plunge frequency for a given mass M, up to the final cutoff frequency due to the lower limit end of the SMBH mass function (compare with the duty cycle $\mathcal{D}(f)$ in Fig. 5).

Note that these event rates are, within orders of magnitude, consistent with independent estimates of EMRIs based on loss cone calculations. Such estimates give inspiral rates of "captured" compact objects per galaxy ranging from $\sim 10^{-7}$ [45] to $\sim 10^{-5}\ {\rm yr}^{-1}$ [46]. With a few billion galaxies out to $z \sim 1$, this corresponds to rates between ~ 100 and $\sim 10^4\ {\rm yr}^{-1}$.

In Fig. 8 we show the unresolvable portion of the GW power spectrum for the fiducial model and a range of m, subtracting out all contributions from systems with SNR >15. Clearly, for larger values of m, the threshold SNR is reached at an earlier time and thus lower frequency in the inspiral, reducing the confusion noise at higher frequencies.

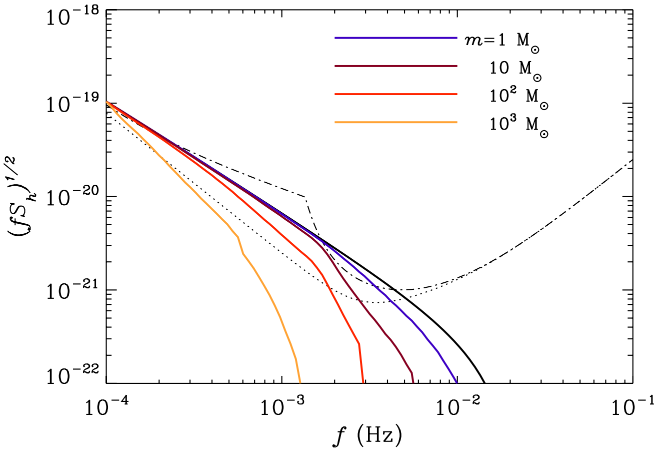

FIG. 8 (color online). Unresolvable GW spectra for a range of compact object masses m, after subtracting out individual events with integrated SNR above a threshold of 15. The solid black curve corresponds to the total time-averaged spectrum, including the resolvable portion.

cies. We notice that even the subtracted events can increase the total noise (26) by an amount proportional to S_n [47], because information used to subtract the events cannot be used to detect other events. However, in our case, we have found that this increase in negligible.

From the dependence $\mathcal{D}(f) \propto f_{\rm co}/m^2$ and from Fig. 5, we can deduce that for fixed $f_{\rm Edd}$ and $\eta_{\rm em}$ and $m \lesssim 10^2(f_{\rm co}/0.01)^{1/2}M_\odot$, the duty cycle is larger than unity and, therefore, the background can basically be treated as Gaussian at all frequencies where a detectable signal is predicted. For $m \gtrsim 10^2(f_{\rm co}/0.01)^{1/2}M_\odot$, the frequency where the duty cycle crosses unity is in a range where $\mathcal{D}(f)$ roughly scales as $f^{-8/3}$ (see Fig. 5), because the inspiral rate $\Gamma(f)$ varies much more weakly (see Fig. 7), and the coherence time, Eq. (31), $t_{\rm coh} \propto f^{-8/3}$. As a result, the GW background becomes Gaussian when

$$f \lesssim f_{\rm Gauss} \simeq 2 \times 10^{-3}\left(\frac{f_{\rm co}}{0.01}\right)^{3/8}\left(\frac{10^2 M_\odot}{m}\right)^{3/4} \text{ Hz}. \qquad (35)$$

Note from Fig. 8 that the frequency below which the background becomes unsubtractable, and thus contributes to confusion noise, is lower by a factor ∼5–10 compared to the frequency Eq. (35) below which the noise becomes Gaussian because the duty factor becomes larger than unity. Figure 8 also shows that the compact object mass above which inspirals tend to become resolvable, $m \gtrsim 10M_\odot$, is comparable to the compact object mass above which the signal consists of individual events (i.e. the duty cycle is smaller than unity). In other words, there is indeed a range of frequencies and compact object masses giving a quasicontinuous signal which may still be resolved into individual events given an improved detector. However, when the duty cycle is much greater than unity, even a perfect detector will not be able to resolve the individual sources, as is the case for most of the galactic white-dwarf population [3].

V. CONCLUSIONS

Assuming scaling relations between accretion rates, intrinsic bolometric and x-ray luminosities, and supermassive black hole mass on the one hand, and rates and masses of compact object inspirals on the other hand, one can predict GW spectra from AGN sources. When part of these scaling relations are constrained observationally, one obtains amplitudes detectable by LISA if the fraction of material accreted in the form of compact objects is $\gtrsim 1\%$. The GW signal depends relatively little on the accretion and emission parameters, as long as these are within the observational constraints. It increases with the fraction of the observed mass density of supermassive black holes that is due to accretion ($f_{\rm Edd}$), and is thus largest for accretion dominated growth.

Our scenarios are well within existing observational upper limits. For example, for the highest flux shown in Fig. 3 one obtains $\Omega_{\rm gw}(10^{-8}{\rm Hz})h_0^2 \lesssim 10^{-12}(f_{\rm co}/0.01)$, compared to the msec pulsar timing limit $\Omega_{\rm gw}(10^{-8}{\rm Hz})h_0^2 \lesssim 10^{-8}$ [48]. This class of sources is not important for future missions sensitive around 1 Hz, such as BBO [49].

If LISA establishes a detection or upper limits on $\Omega_{\rm gw}(f)$, this may be translated into constraints on the parameters $f_{\rm co}$, m, $\eta_{\rm gw}$, $f_{\rm X}$, $f_{\rm Edd}$, and $\eta_{\rm em}$ used in the present parametrization. Since $f_{\rm X}$, $f_{\rm Edd}$, and $\eta_{\rm em}$ are rather well constrained by AGN astronomy, and $\eta_{\rm gw}$ is rather well determined by theory, LISA will mainly constrain $f_{\rm co}$ and m. A more detailed study where these parameters depend on luminosity and/or different AGN classes may allow for more detailed predictions, but is beyond the scope of the present exploratory study.

For compact object masses $m \lesssim 10^2(f_{\rm co}/0.01)^{1/2}M_\odot$, where $f_{\rm co}$ is the fraction of material accreted in form of these compact objects, the background is Gaussian at nearly all frequencies where a detectable signal is predicted. In contrast, for $m \gtrsim 10^2(f_{\rm co}/0.01)^{1/2}M_\odot$, the GW background is Gaussian only at frequencies $f \lesssim 2 \times 10^{-3}(f_{\rm co}/0.01)^{3/8}(10^2M_\odot/m)^{3/4}$ Hz, above which the duty cylce is smaller than unity. The frequency below which the GW background becomes confusion noise because the signal-to-noise ratio becomes too small to subtract out individual events is smaller than this Gaussian frequency by a factor ∼5–10. At higher frequencies one would observe individual coherent signals of typical duration $\simeq 0.2(10^2M_\odot/m)(10^{-3}{\rm Hz}/f)^{8/3}$ yr which occur at a typical rate $\sim 10^2(f_{\rm co}/0.01)(10^2M_\odot/m)$ yr^{-1}. This is typical for supermassive binary inspiral discussed before in the literature.

While the time-averaged GW background described in this paper will be similar to other EMRI backgrounds (e.g. Ref. [14]), the resolvable waveforms should provide information that allows us to distinguish between the circular, equatorial inspirals of disk-embedded objects and the highly inclined, eccentric orbits predicted for capture inspirals. When combined with knowledge of the electromagnetic properties of active galactic nuclei, LISA should be able to constrain primarily the fraction of accretion in form of compact objects and the mass of these compact objects, and thus provide fundamental new insights into the problem of star formation in AGN disks.

ACKNOWLEDGMENTS

We thank Curt Cutler and Joe Silk for useful discussions. G. S. thanks the European Network of Theoretical Astroparticle Physics ILIAS/N6 under Contract No. RII3-CT-2004-506222 for partial financial support and the Physics Department at University of Maryland for hospitality during his visit. A. B. acknowledges support from the Alfred Sloan Foundation.

[1] See, e.g. http://lisa.nasa.gov.

[2] P.L. Bender and D. Hils, Classical Quantum Gravity **14**, 1439 (1997).

[3] N.J. Cornish, Classical Quantum Gravity **18**, 4277 (2001).

[4] J. Goodman and J.C. Tan, Astrophys. J. **608**, 108 (2004).

[5] Y. Levin, astro-ph/0307084; astro-ph/0603583.

[6] Y. Ueda, M. Akiyama, K. Ohta, and T. Miyaji, Astrophys. J. **598**, 886 (2003).

[7] J.-P. De Villiers, J.F. Hawley, and J.H. Krolik, Astrophys. J. **599**, 1238 (2003).

[8] C.F. Gammie, S.L. Shapiro, and J.C. McKinney, Astrophys. J. **602**, 312 (2004).

[9] J.C. McKinney and C.F. Gammie, Astrophys. J. **611**, 977 (2004).

[10] Q.J. Yu and S. Tremaine, Mon. Not. R. Astron. Soc. **335**, 965 (2002).

[11] M. Elvis, G. Risaliti, and G. Zamorani, Astrophys. J. **565**, L75 (2002).

[12] J.-M. Wang *et al.*, Astrophys. J. **642**, L111 (2006).

[13] R. Shafee *et al.*, Astrophys. J. Lett. **636**, L113 (2006).

[14] L. Barack and C. Cutler, Phys. Rev. D **70**, 122002 (2004).

[15] P. Salucci, E. Szuszkiewicz, P. Monaco, and L. Danese, Mon. Not. Royal Acad. Sci. **307**, 637 (1999).

[16] L. Ferrarese and D. Merritt, Astrophys. J. **539**, L9 (2000).

[17] A.C. Fabian and X. Barcons, Annu. Rev. Astron. Astrophys. **30**, 429 (1992).

[18] K.S. Thorne, Astrophys. J. **191**, 507 (1974).

[19] P.F. Hopkins, R. Narayan, and L. Hernquist, Astrophys. J. **643**, 641 (2006).

[20] A.C. Fabian and K. Iwasawa, Mon. Not. R. Astron. Soc. **303**, L34 (1999).

[21] L.L. Cowie *et al.*, Astrophys. J. **584**, L57 (2003).

[22] A. Marconi, G. Risaliti, R. Gilli, L.K. Hunt, R. Maiolino, and M. Salvati, Mon. Not. R. Astron. Soc. **351**, 169 (2004).

[23] A. Merloni, Mon. Not. Royal Acad. Sci. **353**, 1035 (2004).

[24] R. Narayan and I. Yi, Astrophys. J., **428**, L13 (1994).

[25] L. Miller, W.J. Percival, S.M. Croom, and A. Babic, astro-ph/0608202.

[26] J.A. Kollmeier *et al.*, Astrophys. J. **648**, 128 (2006).

[27] M.C. Begelman, Astrophys. J. **568**, L97 (2002).

[28] S. Collin *et al.*, Astron. Astrophys. **388**, 771 (2002).

[29] A. King, Astrophys. J. **596**, L27 (2003).

[30] A. Kogut *et al.*, Astrophys. J. Suppl. Ser. **148**, 161 (2003).

[31] V. Beckmann, N. Gehrels, C.R. Shrader, and S. Soldi, Astrophys. J. **638**, 642 (2006).

[32] C.Y. Peng, C.D. Impey, H.W. Rix, C.R. Keeton, E.E. Falco, C.S. Kochanek, and J. Lehar, New Astron. Rev. **50**, 689 (2006).

[33] M. Enoki and M. Nagashima, astro-ph/0609377.

[34] C. Casalvieri, V. Ferrari, and A. Stavridis, Mon. Not. R. Astron. Soc. **365**, 929 (2006).

[35] R. Narayan, Astrophys. J. **536**, 663 (2000).

[36] S.K. Chakrabarti, Phys. Rev. D **53**, 2901 (1996); P.J. Armitage and P. Natarajan, Astrophys. J. **567**, L9 (2002).

[37] S.L. Shapiro and S.A. Teukolsky, *Black Holes, White Dwarfs, and Neutron Stars: The Physics of Compact Objects* (Wiley-Interscience, New York, 1983).

[38] K.S. Thorne, in *300 Years of Gravitation*, edited by S.W. Hawking and W. Israel (Cambridge University Press, Cambridge, England, 1987), pp. 330–458.

[39] E.S. Phinney, astro-ph/0108028.

[40] L.S. Finn and K.S. Thorne, Phys. Rev. D **62**, 124021 (2000).

[41] E.E. Flanagan and S.A. Hughes, Phys. Rev. D **57**, 4535 (1998).

[42] H. Netzer and B. Trakhtenbrot, astro-ph/0607654.

[43] P.C. Peters, Phys. Rev. **136**, B1224 (1964).

[44] S. Drasco and E.E. Flanagan, Phys. Rev. D **67**, 082003 (2003).

[45] C. Hopman and T. Alexander, Astrophys. J. **645**, L133 (2006).

[46] K. Holley-Bockelmann and S. Sigurdsson, astro-ph/0601520.

[47] C. Cutler (private communication).

[48] S. Thorsett and R. Dewey, Phys. Rev. D **53**, 3468 (1996).

[49] E.S. Phinney *et al.* (The Big Bang Observer), NASA Mission Concept Study, 2003;http://universe.nasa.gov/program/vision.html.